

## Article

# Computational-Fluid-Dynamics-Based Optimization of Wavy-Slit Fin Geometry in Indoor Units of Air Conditioners Using Low-Global-Warming-Potential Refrigerants

Jaewon Roh, Youngseo Kim and Joon Ahn \* 

School of Mechanical Engineering, Kookmin University, 77 Jeongneung-ro, Seongbuk-gu, Seoul 02707, Republic of Korea; cxzpoiuy@kookmin.ac.kr (J.R.); tj1351@kookmin.ac.kr (Y.K.)

\* Correspondence: jahn@kookmin.ac.kr

**Abstract:** This study explores the optimization of wavy-slit fins in the indoor units of air conditioners that use low-global-warming-potential refrigerants, with a focus on the interactions between slit length, width, and height. A response surface method was employed to analyze the trade-offs between thermal performance and pressure loss, and numerical optimization was performed using two objective functions: pumping power and volume goodness factor (Gv). The results demonstrated that optimizing the slits' geometry significantly enhanced overall performance. For pumping power, a minimum point was observed near the design boundaries, which underscores the critical role of geometric interactions. The flow and temperature field analysis under fixed heat-duty conditions revealed substantial flow separation caused by the slits, enhanced mixing between the upper and lower surfaces, and a reduction of up to 2.05% in pumping power. In contrast, the Gv optimization model exhibited a more uniform flow, reducing flow separation beyond the pipe and improving the Gv by 1.85%, although it led to an increase in pumping power. These findings highlight the potential that tailored slit fin designs have to achieve a balanced enhancement in heat transfer and aerodynamic performance, offering valuable insights for the development of efficient, low-environmental-impact air conditioning systems.

**Keywords:** wavy-slit fin; low-global-warming-potential refrigerant; response surface method; volume goodness factor; computational fluid dynamics



check for updates

Academic Editors: Cesare Biserni, Junhong Park and Guillermo Hauke

Received: 16 September 2024

Revised: 21 January 2025

Accepted: 22 January 2025

Published: 24 January 2025

**Citation:** Roh, J.; Kim, Y.; Ahn, J. Computational-Fluid-Dynamics-Based Optimization of Wavy-Slit Fin Geometry in Indoor Units of Air Conditioners Using Low-Global-Warming-Potential Refrigerants. *Appl. Sci.* **2025**, *15*, 1196. <https://doi.org/10.3390/app15031196>

**Copyright:** © 2025 by the authors. Licensee MDPI, Basel, Switzerland. This article is an open access article distributed under the terms and conditions of the Creative Commons Attribution (CC BY) license (<https://creativecommons.org/licenses/by/4.0/>).

## 1. Introduction

Global warming due to climate change has emerged as a critical issue worldwide. According to reports from the Intergovernmental Panel on Climate Change (IPCC), greenhouse gas emissions have been identified as a primary driver of global warming [1], with the refrigerants used in air-conditioning systems being highlighted as one of the major contributors [2]. The HCFC and CFC refrigerants that were commonly used in the past were found to cause ozone depletion and were subsequently restricted by the Montreal Protocol, which came into effect in 1987. They have since been replaced by refrigerants with zero ozone depletion potential (ODP), such as HFCs. However, these zero ODP refrigerants have high global warming potential (GWP) and contribute to global warming when released into the atmosphere. Through various climate agreements, the use of refrigerants with high GWP is being increasingly restricted [3], and research is being conducted on low-GWP refrigerants as alternatives to these [4,5].

As refrigerants are replaced, changes in their thermophysical properties affect the heat transfer performance of heat exchangers [6]. In response, studies have been conducted to

determine how heat transfer performance can be improved by adopting smaller-diameter tubes in the evaporators of air conditioners that use low-GWP refrigerants, thereby increasing the heat transfer area of the heat exchangers [7]. Additionally, since the air-side resistance accounts for over 90% of the total thermal resistance in fin-tube heat exchangers [8], various studies have investigated how air-side heat transfer can be enhanced by optimizing fin designs [9].

Several fin designs have been employed to enhance air-side heat transfer in the indoor units of air conditioners; common types include louvered fins, slit fins, and wavy fins. Dimensionless numbers, such as the *j*-factor and *f*-factor, are commonly used to evaluate the performance of different fin types. The *j*-factor, derived from the Stanton and Prandtl numbers, represents heat transfer performance, while the *f*-factor quantifies frictional losses and pressure drop across the fin [10]. Yun et al. [11] experimentally compared the heat transfer and pressure drop characteristics of plain fins, slit fins, and louvered fins to find that the slit fin exhibited the highest *j*-factor while the louvered fin had the highest *f*-factor. Despite the louvered fin's higher *f*-factor, the slit fin demonstrated superior performance in terms of heat transfer and pressure drop due to its higher *j*-factor. Youn et al. [12] conducted experiments comparing the heat transfer coefficient and friction factor of sinusoidal-wave fins and herringbone-wave fins. They found that, at the same waffle height, the sinusoidal-wave fin demonstrated higher heat transfer and friction coefficients as well as a faster transition to turbulence.

Research has also been conducted on wavy-slit fins, which combine the characteristics of wave fins and slit fins. Youn et al. [13] demonstrated that wavy-slit fins exhibit a higher heat-transfer-enhancement effect compared to wave fins. Mohanta et al. [14] used computational fluid dynamics (CFD) to compare the thermohydraulic performance of wavy fins and wavy-slit fins, revealing that the *j*-factor of wavy-slit fins improved by 20–39% compared to wavy fins, although the *f*-factor also increased by 20–38%. Therefore, it is necessary to optimize fin geometry based on an objective function that considers both heat transfer and pressure drop to achieve optimal performance.

Studies on shape optimization typically involve fabricating multiple models with different geometric parameters and then conducting experiments to derive the optimal point statistically based on the results. This process can be time-consuming and expensive, but these challenges can be mitigated using CFD. Additionally, using CFD allows for the analysis of localized flow and temperature distributions, which helps identify the mechanisms responsible for improved performance in the optimal geometry. Therefore, CFD has been extensively utilized for the optimization of fin shapes for air conditioners [15].

Liu et al. [16] optimized the geometric parameters of fins using CFD to enhance the heat transfer performance of the herringbone wavy-slit heat exchanger. The geometric parameters selected were waffle height, fin pitch, and wavelength, and the optimal design was determined based on these variables. Li et al. [17] simulated the heat transfer and fluid flow of a wavy fin-tube heat exchanger equipped with delta-winglet-type vortex generators (VGs). The corrugation height of the fins and the attack angle of the delta-winglet VGs were optimized using the CFD results, with the Colburn *j*-factor and *f*-factor as the respective objective functions.

Liu et al. [16] considered only the wavy shape in their study. However, for wavy-slit fins, the geometric parameters of the slits also affect heat transfer and flow characteristics. The variations that occur in recirculation zones and vortex generation due to these parameters directly impact heat transfer performance [14]. Additionally, the heat transfer area of the fins changes based on the height, width, and length of the slits. While research has been conducted on the effects of the geometric parameters of slits in wavy-slit fins [18], there

have been no studies that have explored the notion of optimizing these fins by considering the comprehensive effects of their geometric parameters.

An analytical validation of small-diameter wavy-slit fins was carried out by Lee [19]. Subsequently, in the study by Park and Kang [20], the effects of various factors were analyzed with the aim of improving performance. The impact of the three slit factors (length, width, and height) on heat and pressure indicated that as the slit height increased, both the  $j$ - and the  $f$ -factor initially increased and then decreased after reaching optimal values, whereas, as the slit width increased, the reduction in the  $j$ - and  $f$ -factor became less pronounced. Finally, as the slit length increased, the  $j$ -factor initially increased but then decreased, while the  $f$ -factor continued to increase, exhibiting a differing trend. No significant correlation was found between the shape factors and the  $j$ - and  $f$ -factor, and the shapes optimized based on their performance in each individual setting did not achieve optimal performance due to the interactions among the factors [19,20]. Therefore, this study introduced the response surface method (RSM) [21,22] to carry out optimization for two objective functions.

As done in a previous study [20], the longitudinal pitch ( $P_l$ ) and transverse pitch ( $P_t$ ) of the wavy-slit fin (shown in Figure 1) were fixed, while the slit length ( $L$ ), width ( $W$ ), and height ( $H$ ) were taken as geometric variables. Using the RSM, various shapes were generated by combining the geometric variables  $L$ ,  $W$ , and  $H$ , and a CFD analysis was performed. Two objective functions were considered for optimization. First, the reduced pumping power function was established, which minimizes pumping power while maintaining a fixed heat transfer rate, as suggested by Soland et al. [23] and Shah et al. [10]. Second, the volume goodness factor ( $G_v$ ), defined by Webb et al. [24] to achieve the maximum heat exchange rate for a given volume and pumping power [25], was set as the objective.

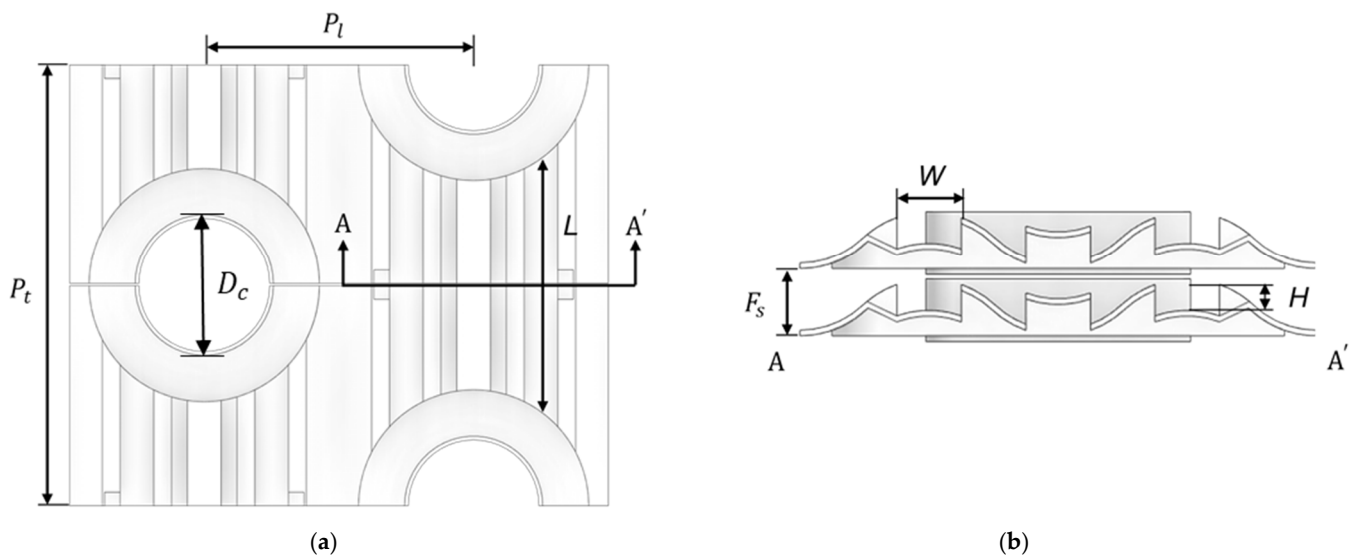


**Figure 1.** Geometric shape and parameters of the wavy-slit fin analyzed in this study. (a) Top view (b) Side view.

In this study, the geometric variables of the slits in wavy-slit fins, which were intended for use in small-diameter indoor evaporators of air conditioners with low-GWP refrigerants, were optimized using the RSM. This paper presents two optimized shapes that were obtained using reduced pumping power and  $G_v$  as the objective functions. The flow and temperature fields of the reference shape and the two optimized shapes have been compared to review the mechanisms through which performance is improved according to the objectives. To verify the heat transfer and pressure drop performance under partial

load conditions, the Colburn  $j$ - and  $f$ -factor, as functions of flow rate, are presented for the two optimized shapes.

## 2. Materials and Methods

### 2.1. Modeling and CFD Methodology

The 3D model of the wavy-slit fin employed in this numerical analysis is illustrated in Figure 2a. The 3D model was created using Creo 6.0.6.0, and the geometric parameters of the fins are provided in Table 1.

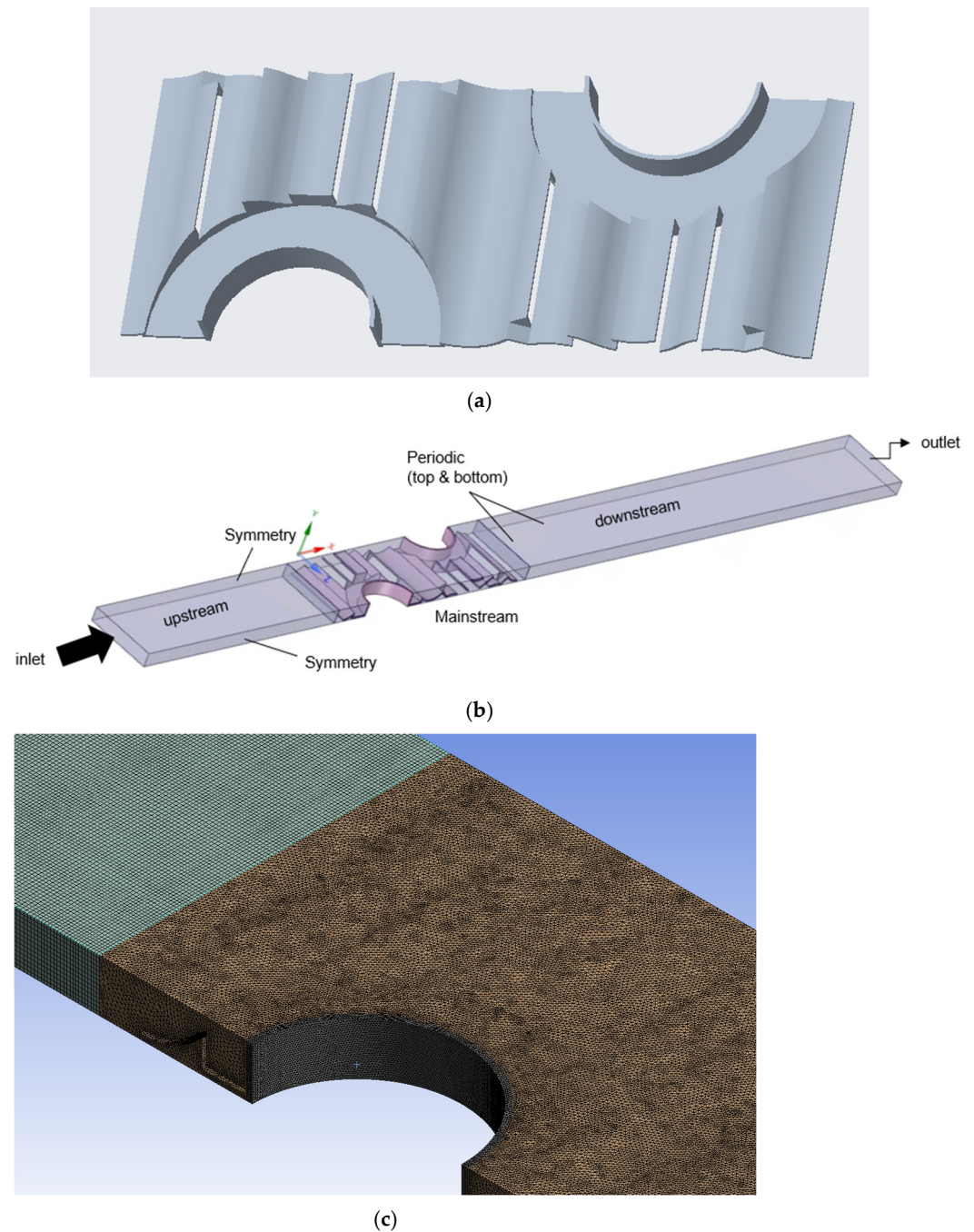


**Figure 2.** Modeling and meshing setup for CFD simulations. (a) 3D model of wavy-slit fin (b) Computational domain and boundary conditions (c) Grid system.

**Table 1.** Geometric dimensions of the fins.

Design Parameters	Range (mm)
Fin pitch ( $F_s$ )	1.25
Transverse tube pitch ( $P_t$ )	16.7
Longitudinal tube pitch ( $P_l$ )	10.3
Collar outer diameter ( $D_c$ )	5.28
Slit length ( $L$ )	7.9~13.6
Slit width ( $W$ )	0.8~1.8
Slit height ( $H$ )	0.3125~0.8

To ensure sufficient flow development, convergence, and result accuracy, we extended the computational domain based on the reference length of 22.6 mm, which corresponds to the length of the region occupied by the heat exchanger within the computational domain, as outlined in [26]. The upstream was extended one time and the downstream two times this length. The configuration of the computational domain, including these extensions, was pretested and validated in a previously published study. For the boundary conditions in the numerical analysis, with the y-direction corresponding to the fin pitch direction as the reference, symmetry conditions were applied to both sides, and periodic conditions were imposed on the top and bottom. A velocity boundary condition was applied at the inlet, with the inlet velocity varying between 0.5 and 1.5 m/s, and the temperature was set to 284.95 K. The inlet turbulence conditions were specified using the intensity and length scale method, with a turbulence intensity of 1%, based on the experimental results of the suction fan that generates the airflow. The turbulence length scale was set to 1 mm, consistent with the characteristic length of the geometry. Pretesting showed that varying the turbulence length scale between 0.1 mm and 10 mm resulted in no significant differences in the simulation results, ensuring the robustness of the selected value. An atmospheric pressure condition was applied at the outlet (Figure 2b).

The refrigerant flows within the tube, exchanging heat with the fins. Convective heat transfer boundary conditions were applied to the inner surface of the tube, with a heat transfer coefficient of 8000 W/m<sup>2</sup> and a temperature of 307.5 K. Additionally, the wall boundary condition was set to a no-slip condition. The physical phenomenon of the airflow under analysis was a 3D incompressible, steady-state-convection heat transfer problem. The governing equations are the time-averaged mass conservation equation, momentum equation, and energy equation [27].

- Continuity equation

$$\frac{\partial}{\partial x_i}(\rho U_i) = 0 \tag{1}$$

- Momentum equation

$$\frac{\partial}{\partial x_j}(\rho U_i U_j) = -\frac{\partial P}{\partial x_i} + \frac{\partial}{\partial x_j} \left( \mu \left( \frac{\partial U_i}{\partial x_j} + \frac{\partial U_j}{\partial x_i} \right) \right) - \frac{\partial}{\partial x_j}(\rho \langle u_i u_j \rangle) \tag{2}$$

- Energy equation

$$\frac{\partial}{\partial x_j}(\rho c_p U_j T) = \frac{\partial}{\partial x_j} \left( k \frac{\partial T}{\partial x_j} \right) - \frac{\partial \rho c_p \langle u_j t \rangle}{\partial x_j} \tag{3}$$

The numerical analysis was conducted using the commercial software Ansys Fluent 2020 R1, which was used to perform incompressible Reynolds-averaged Navier–Stokes (RANS) simulations. The discretization method employed was the second-order upwind

scheme, and pressure-velocity coupling was handled using the SIMPLE algorithm. Convergence was determined when all residuals fell below  $1 \times 10^{-6}$  after performing more than 8000 iterations [28].

## 2.2. Objective Function

Heat exchangers involve a trade-off between pressure performance and thermal performance, making it necessary to set objectives and optimize toward those goals. The performance indicators—heat transfer rate ( $Q$ ) and pumping power ( $P$ )—were specified according to the definitions provided by Shah [10]. The computational domain in Figure 2b considers one fin, and the total number of fins can be calculated, as shown in Equation (4).

$$N_d = \frac{L_{HTX}}{P_t} \quad (4)$$

Using this approach, the heat transfer rate and pumping power can be calculated, as shown in Equations (5) and (6).

$$Q = \frac{\dot{m}c_p\Delta T}{F_p}N_d \quad (5)$$

$$P = \frac{\Delta P\dot{m}}{\rho F_p}N_d \quad (6)$$

The first objective function, reduced pumping power, was selected with the aim of minimizing the pumping power calculated in Equation (6). The dimensionless numbers for heat transfer and pressure drop, known as the  $j$ - and  $f$ -factor, are defined as follows:

$$j = \text{StPr}^{\frac{2}{3}} \quad (7)$$

$$f = \frac{A_c 2\Delta P}{A_0 \rho V_m^2} \quad (8)$$

The maximum velocity  $V_m$  was calculated based on the flow rate at the smallest cross-sectional area  $A_c$ . Further, the Reynolds number was also defined using the average velocity in this area.

$$V_m = \frac{\dot{m}_{ac}}{\rho A_c} \quad (9)$$

$$\text{Re}_{Dc} = \frac{V_m D_c}{\mu} \quad (10)$$

The second objective function, the volume goodness factor, was selected from the goodness factors proposed by Webb [24], and it used the dimensionless numbers  $j$  and  $f$  presented in Equations (7) and (8). The volume goodness factor is defined as a performance indicator utilized to maximize volume performance for components used in fixed air-conditioning units while considering the trade-off between the  $j$ - and  $f$ -factor values [25].

$$\text{Gv} = \frac{\text{St}}{f^{\frac{1}{3}}} \quad (11)$$

## 2.3. Validation of Numerical Analysis

The mesh was generated using Ansys Meshing, as shown in Figure 2c. Tetrahedral meshes were used for the tube and mainstream regions, while structured meshes were employed for the remaining areas. The grid resolution near the wall was evaluated using wall coordinates. In most regions, the  $y^+$  value is below 0.1, with a local maximum of 1.1. Further, a mesh sensitivity analysis was conducted to determine the appropriate mesh resolution [28]. Meshes with one million, four million, six million, seven million, eight

million, and nine million cells were created and analyzed. The results of the *j*-factors for each mesh size are illustrated in Figure 3. Based on the mesh sensitivity analysis, a mesh size of seven million cells was selected, as it showed negligible error for the *j*-factor.

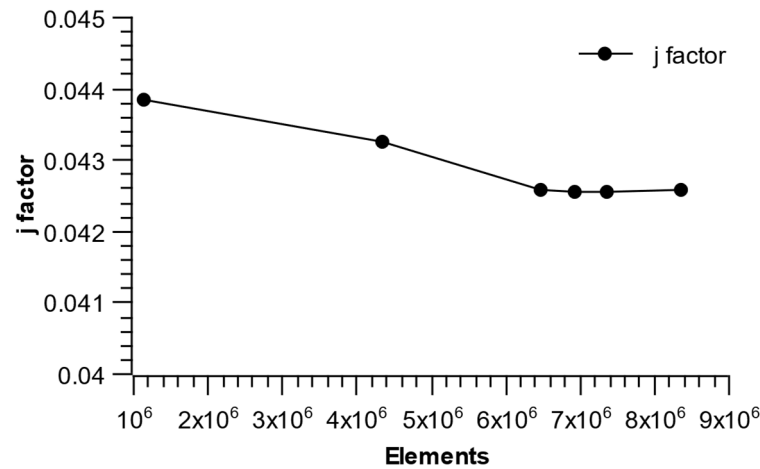


Figure 3. Grid sensitivity analysis: number of grids required for converged *j*-factor results.

Results obtained using the standard *k-ε* and *k-ω* SST turbulence models were compared to select the turbulence model. The *j*- and *f*-factor results for both models are compared in Figure 4. While there was no significant difference between the two turbulence models, the *k-ω* the SST model was chosen for this study due to its advantages in predicting boundary layer flow near walls and shear stresses as well as its relative accuracy in predicting adverse pressure gradients and flow separation [29]. The flow structure analyzed in this study exhibits characteristics that differ significantly from the classical laminar-to-turbulent transition scenarios observed on flat plates. With a Reynolds number below 1000, the base flow remains predominantly laminar. However, the turbulence-enhancing effects of the wavy slit fin generate localized turbulence near the slits, which dissipates as the flow moves downstream.

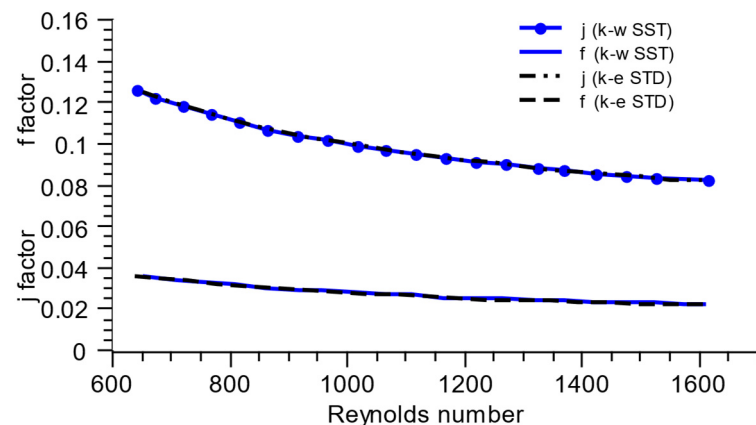
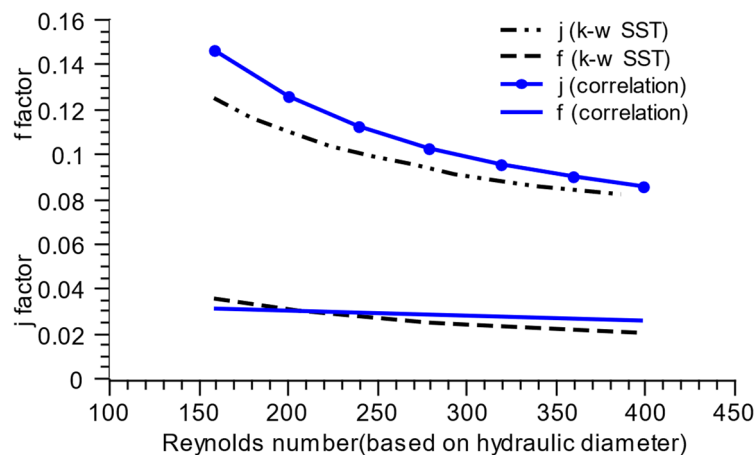


Figure 4. Comparison of the *j*- and *f*-factor across Reynolds numbers: independence from turbulence models.

To accurately capture this behavior, we conducted simulations using the laminar model, the Low Reynolds *k-ε* model, the *k-ε* model with Enhanced Wall Treatment, and the *k-ω* SST model. The comparison of results showed a relative error of only 0.2% for the *j*-factor and within 2% for the *f*-factor, indicating minimal differences between the models. These results suggest that while localized turbulence occurs, it has a negligible impact on the mean flow and overall thermal performance metrics in the region of interest.

Consequently, the steady-state assumption is appropriate for the flow regime investigated in this study.

The *j*- and *f*-factor obtained from the numerical analysis were compared with the experimental correlations from the work of Yoon [13], as shown in Figure 5. The comparison revealed that the *j*-factor exhibited an error of under 5%, while the *f*-factor had an error of under 10%.



**Figure 5.** Validation of CFD results: comparison of the *j*- and *f*-factor with empirical correlations across Reynolds numbers.

#### 2.4. Optimization Process Based on the RSM

First, it is necessary to determine the influence of the factors to identify the optimal point in the RSM. After this is accomplished, a model can be established, and experiments can be conducted to obtain the response variables [30]. In the study conducted by Park and Kang [20], three factors that influence the heat transfer and pressure drop mechanisms were included in the model. Using a central composite design based on the center points and design range, 15 experimental points were determined, as shown in Table 2. A numerical analysis was then conducted for each case to obtain the response variables  $\Delta T$  and  $\Delta P$ .

**Table 2.** Geometric parameters of the RSM cases and experimental data.

Case Number	<i>L</i> (mm)	<i>W</i> (mm)	<i>H</i> (mm)	$\Delta T$ (K)	$\Delta P$ (Pa)
1	7.9	0.8	0.3125	17.3406	27.29
2	13.6	0.8	0.3125	15.5593	35.63
3	7.9	1.8	0.3125	16.894	22.71
4	13.6	1.8	0.3125	15.1377	25.94
5	7.9	0.8	0.8	18.38	31.53
6	13.6	0.8	0.8	17.2649	40.6
7	7.9	1.8	0.8	18.7918	32.23
8	13.6	1.8	0.8	18.4825	43.44
9	7.9	1.3	0.55625	18.6005	28.72
10	13.6	1.3	0.55625	18.048	37.51
11	10.75	0.8	0.55625	19.3582	38.69
12	10.75	1.8	0.55625	19.3201	35.66
13	10.75	1.3	0.3125	18.3369	32.74
14	10.75	1.3	0.8	19.4143	38.99
15	10.75	1.3	0.55625	19.369	37.05

### Regression and Objective Function Optimization

A regression equation associated with the effect of the objective functions  $P$  and  $G_v$  on the three shape factors was formulated as a second-order regression model to evaluate the relationship between the response variables and factors based on the numerical analysis, as shown in Equations (12) and (13) [22]. The regression was performed, and the residuals were verified to confirm that the regression was conducted correctly. The objective function  $P$  was modified to minimize the required fan power while preventing a reduction in thermal performance to achieve optimization, and the  $Q$  value of the reference shape was used as a constraint. This resulted in creating a transformed objective function for reduced pumping power. The optimization of  $G_v$  was carried out in a direction that maximizes  $G_v$ .

$$P = -0.00706 + 0.003404L - 0.00412W - 0.00128H - 0.000145L^2 + 0.00036W^2 - 0.00538H^2 - 0.000081LW + 0.000492LH + 0.00572WH \tag{12}$$

$$G_v = -0.1145 + 0.03217L - 0.0090W + 0.0907H - 0.001712L^2 - 0.00165W^2 - 0.0872H^2 + 0.000911LW + 0.001510LH + 0.01122WH \tag{13}$$

## 3. Results and Discussion

### 3.1. Optimization of Geometric Variables Using the RSM

Before proceeding with the optimization process, the suitability of the current constraint ranges was checked by fixing one parameter at the central points  $W = 1.3$  mm,  $H = 0.55625$  mm, and  $L = 10.75$  mm and presenting the response surface plots that illustrated the relationships between the other two parameters and the objective functions  $P$  and  $G_v$  in Figure 6. Stationary points were observed in both the  $P$  and the  $G_v$  response surface plots.

For  $P$  (Figure 6a), stationary points were observed for the  $L$  and  $H$  relationship, saddle points were found for the  $L$  and  $W$  relationship, and only a descending ridge was present for the  $W$  and  $H$  relationship. For  $G_v$  (Figure 6b), optimal points were found in the middle of the parameter range for  $L$  and  $H$ , stationary points were observed for  $L$  and  $W$ , and only stationary points were present for  $W$  and  $H$ . However, the descending ridge in  $P$  suggests that the optimal point may lie outside the experimental range [22]. The range for  $H$  is limited to 0.3125–0.8 mm due to constraints related to shape fabrication, so the experimental range could not be extended further.

The optimization of the shape factors for the objective functions—reduced pumping power and  $G_v$ —was conducted. The optimized shapes derived using the RSM are shown in Figure 7. For the shape of the reduced pumping power function, at the optimal point,  $L$  decreased by 0.3325 mm, and  $H$  decreased by 0.67205 mm, while  $W$ , which had a relatively minor effect, increased by 0.23061 mm. For the shape of the  $G_v$  function, at the maximum point,  $L$  increased by 0.903 mm,  $W$  increased by 1.17 mm, and  $H$  decreased by 0.5539 mm (see Table 3).

**Table 3.** Geometric parameters of the optimal shape obtained for each objective function.

Configuration	$L$ (mm)	$W$ (mm)	$H$ (mm)
Reference	9.3	0.63	0.625
Reduced pumping power	8.9675	0.86061	0.607955
$G_v$	10.203	1.8	0.7261

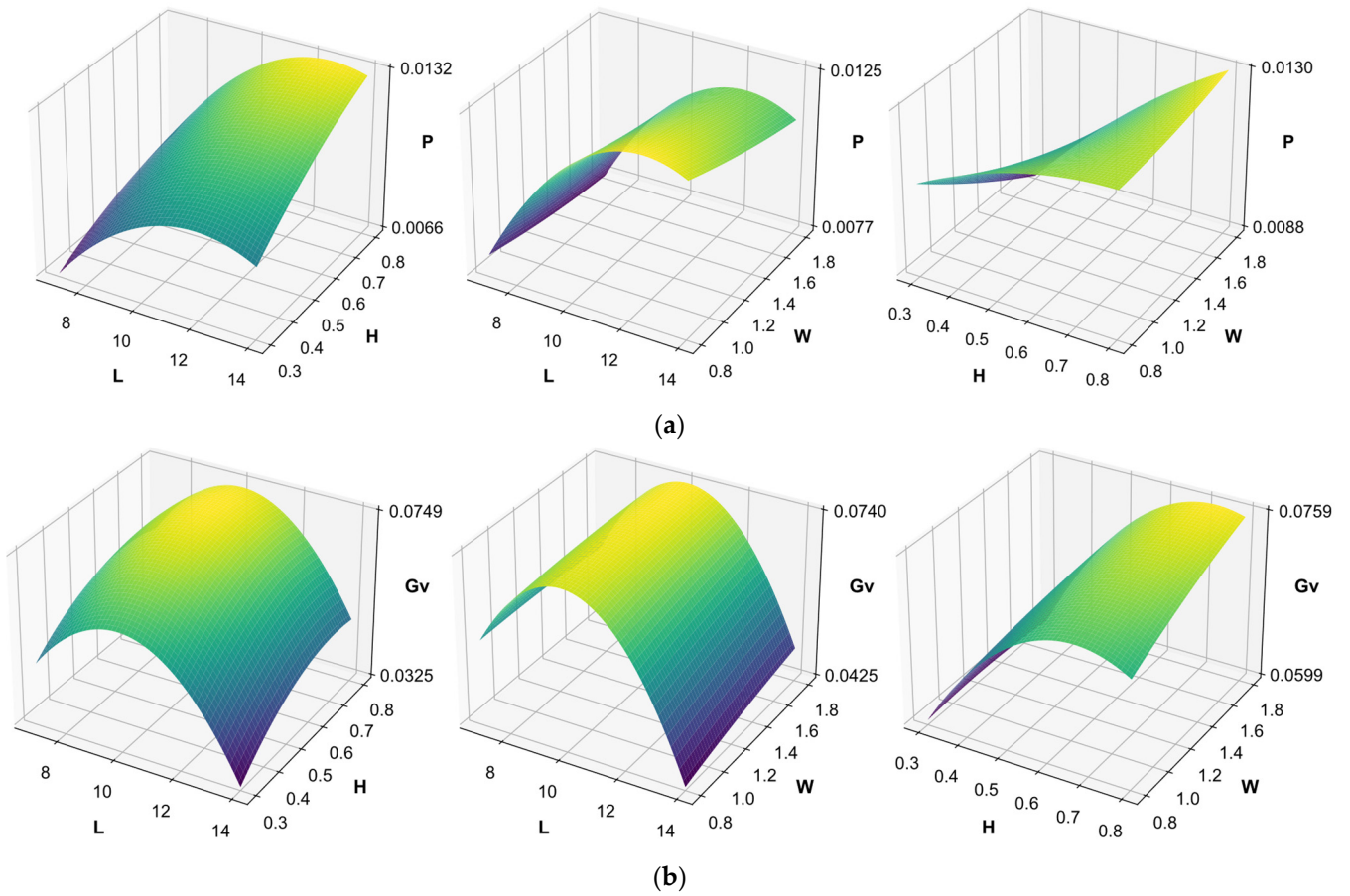


**Figure 6.** Response surface contour plots: objective function analysis for two variables. (a) Pumping power ( $P$ ). (b) Volume goodness factor ( $G_v$ ).

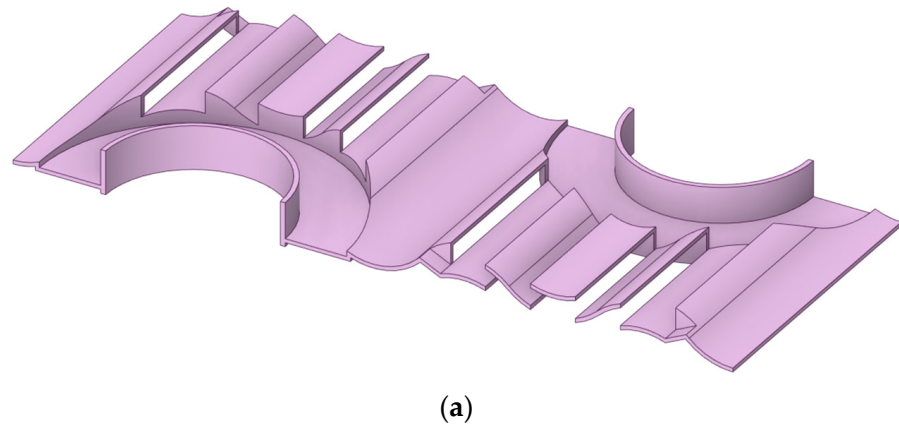


**Figure 7.** Cont.

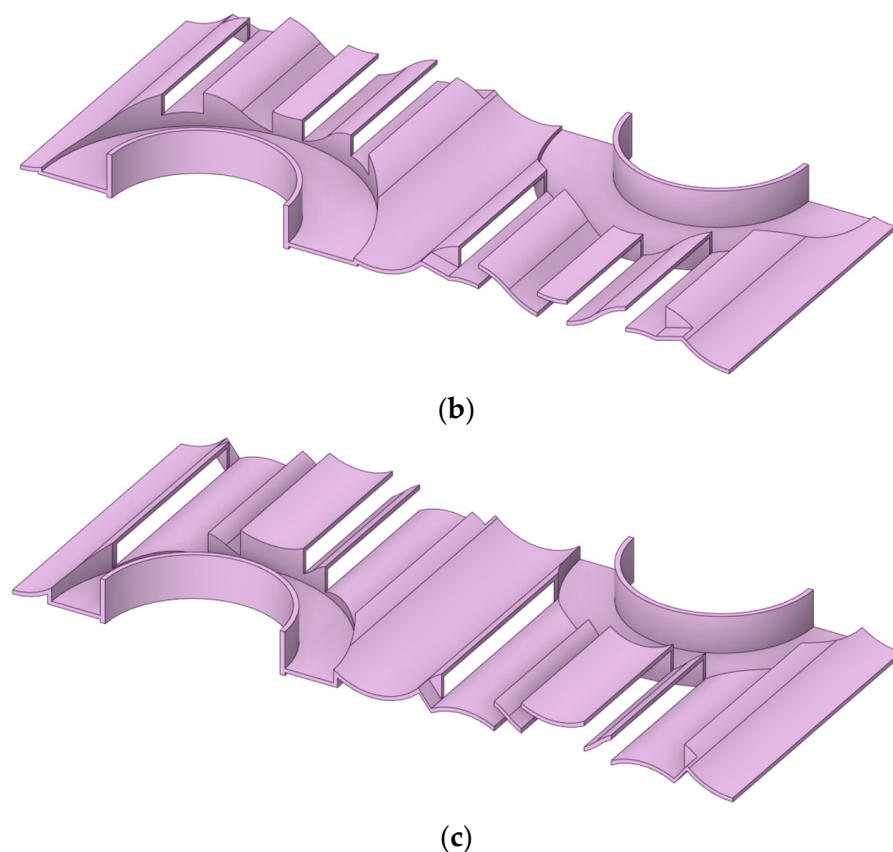


**Figure 7.** Comparison of optimized wavy-slit fins for two objective functions with the reference geometry. (a) Reference geometry. (b) Optimized fin with reduced pumping power. (c) Optimized fin with volume goodness factor.

### 3.2. CFD Analysis of Flow and Thermal Fields in Optimized Geometries

In this section, to illustrate the performance improvement mechanisms, we compare the local flow and thermal fields of the optimized shapes obtained using the RSM at a wind speed of 1.5 m/s with those of the reference shape. Figure 8 shows the flow fields viewed from the surface near the top and bottom of the fin and from the side. For all three shapes, the boundary layer detaches and re-attaches as the flow passes through the slit in the general area. Beyond the forward stagnation point, the laminar boundary layer develops, leading to separation and the observation of a wake and vortices. However, differences were observed among the three shapes in the size of the forward stagnation point and separation zone, as well as in the mixing characteristics of the flow over the upper and lower surfaces through the slit.

First, in the reference shape (Figure 8a), the incoming flow at the front of the first tube row develops a laminar boundary layer at the forward stagnation point, and the main flow passes over the tube at a high velocity of 5 m/s. The stagnation point forms at the center of the tube, after which separation occurs, causing the main flow to split upward and downward as it strikes the slit. The flow passing over the upper surface develops a separation layer, while the flow that has been diverted to the lower surface affects the slit of the next row. A similar flow pattern is observed at the second tube row, but after that, the absence of fins leads to wake formation and the development of vortex layers. The flow passing through the slit fluctuates in the y-direction, creating a velocity difference of more than 1.5 m/s.

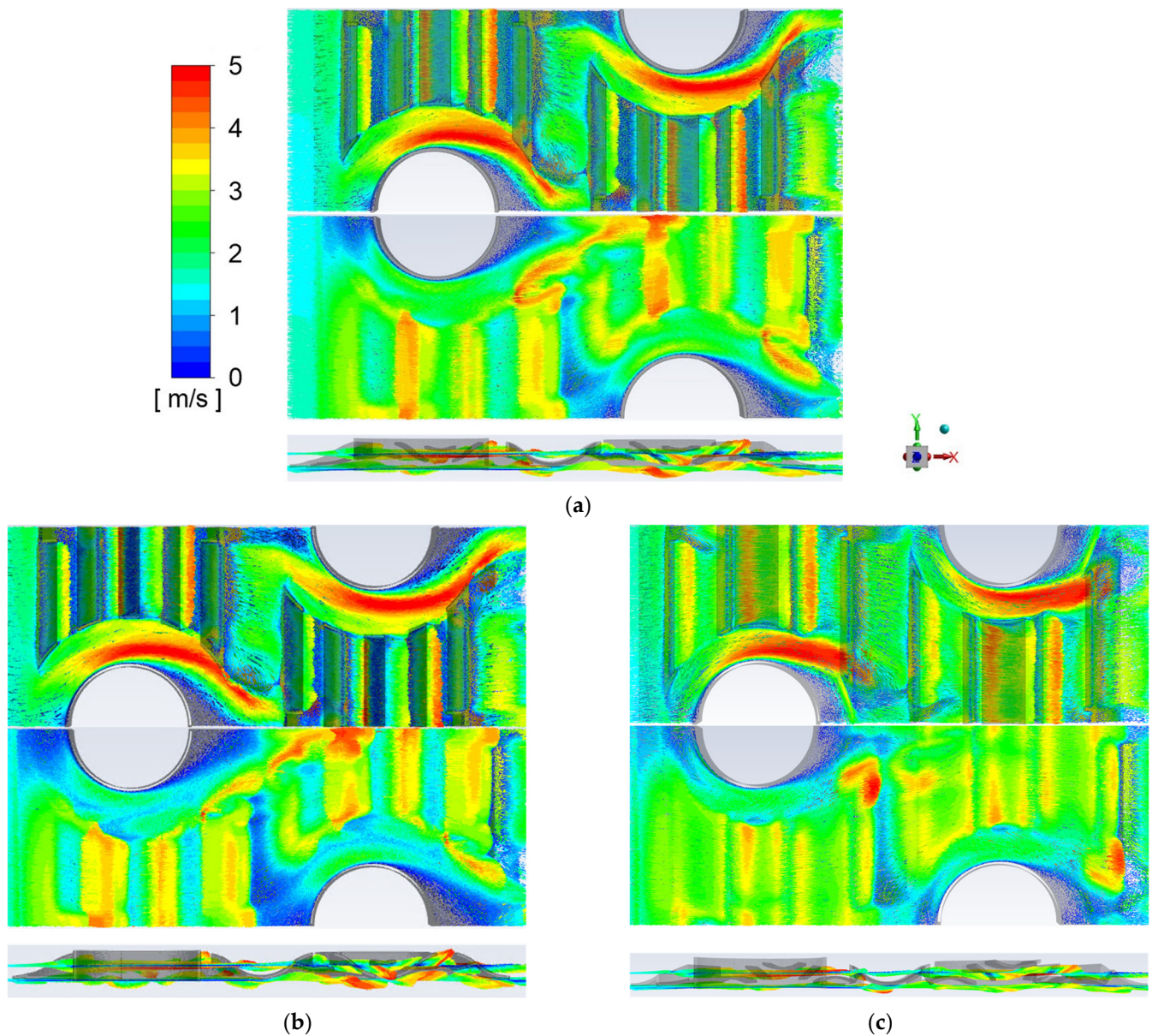


**Figure 8.** Flow comparison around optimized wavy-slit fins for two objective functions and reference geometry. (a) Reference. (b) Optimized fin with reduced pumping power. (c) Optimized fin with volume goodness factor.

In the reduced-pumping-power shape (Figure 8b), the greatest amount of flow enters from the front of the first tube row, and a significant impact can be observed at the stagnation point on the lower surface. In this case, the separation zone develops more significantly than in the reference shape, and the two bifurcated main flows dominate the lower surface, which results in an uneven flow pattern. Strong vortices form after the second tube row, and the flow entering through the slit is less than that of the reference shape, causing the flow velocity on the lower surface to slow down to 0.5–1 m/s.

In the Gv shape (Figure 8c), due to the increased slit length ( $L$ ) compared to the reference shape, the amount of flow entering over the first row of tubes decreases, and the development of vortices and the laminar boundary layer at the stagnation point are delayed. The main flow passing through the slit has a reduced separation layer and, due to the lower velocity, moves along the lower surface. Additionally, the increased slit height ( $H$ ) leads to a greater height in the region between slits, allowing for the development of

relatively uniform flow. After the second row of tubes, wake flow continues, and the flow passing through the slit forms a uniform pattern over both the upper and lower surfaces.

The heat transfer coefficients on the fin surfaces have been compared in Figure 9 to verify the heat transfer distribution of the reference shape and optimized shapes at an inlet velocity of 1.5 m/s. In the velocity distribution of all three shapes, recirculation zones form near the tube after flow separation, resulting in areas of low heat transfer near the tube in the heat transfer coefficient distribution. Additionally, since the flow is divided by the slits, the heat transfer is locally higher at the front of each slit.

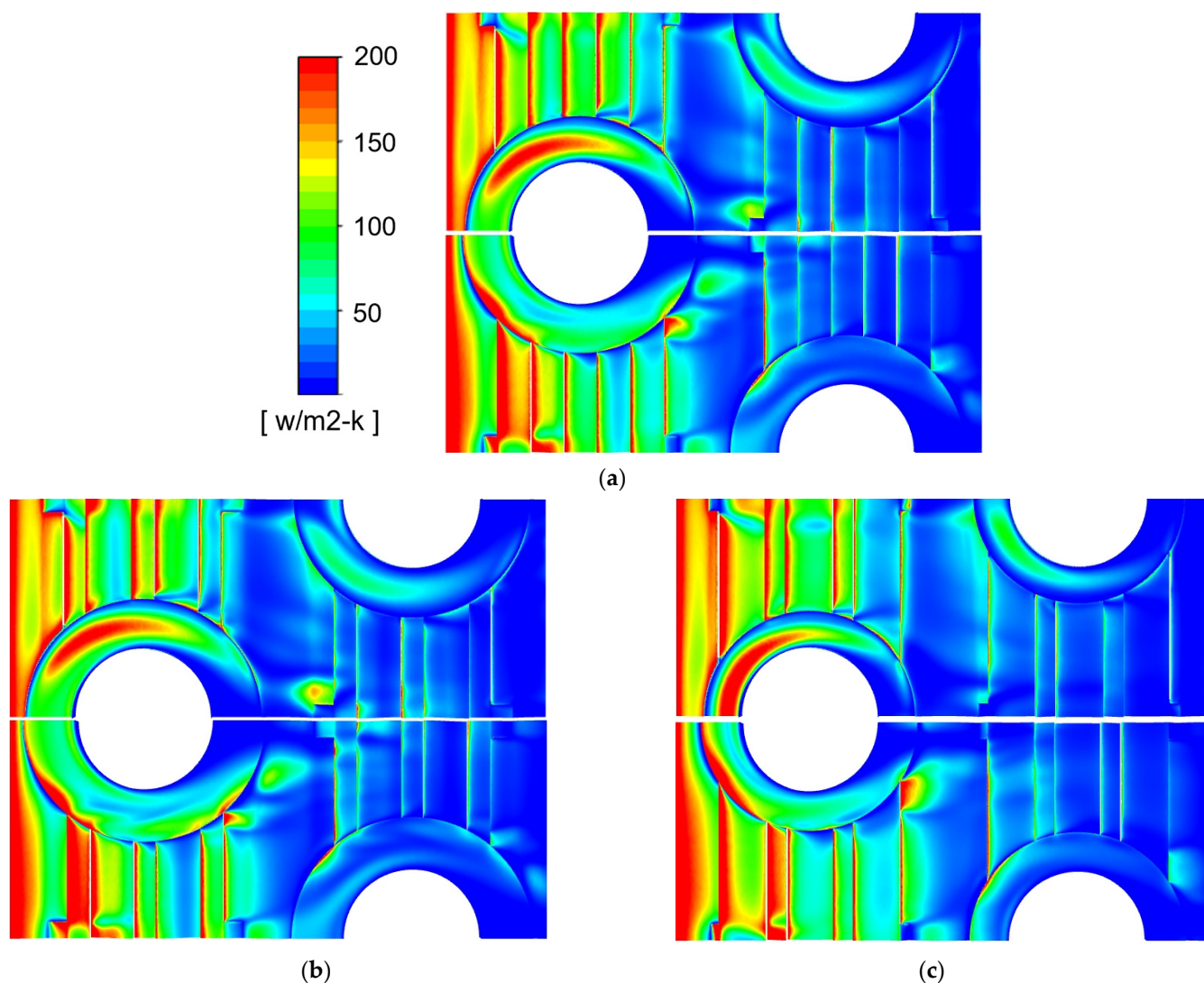


**Figure 9.** Local heat transfer distributions on the surface of optimized and reference wavy-slit fins for two objective functions. (a) Reference. (b) Optimized fin with reduced pumping power. (c) Optimized fin with volume goodness factor.

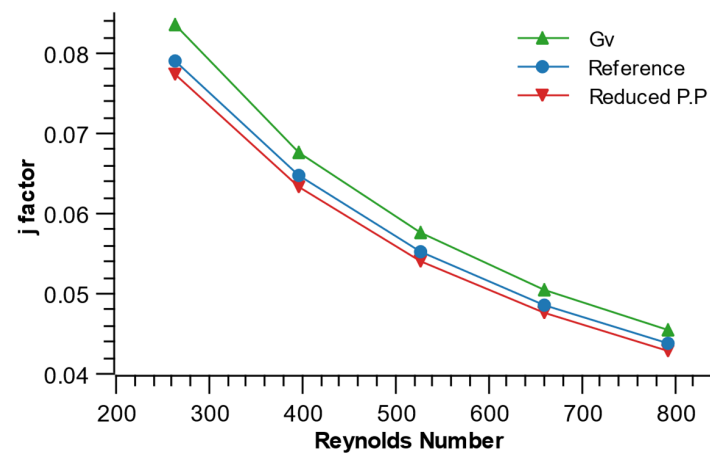
The heat transfer distribution was relatively uneven in the case of the reduced-pumping-power shape (Figure 9b). There were localized regions of high heat transfer at the boundary where the slit begins, but most areas beyond the slit showed low heat transfer. After the first row of tubes, the main flow and the branched flow develop strongly underneath the fin, leading to the creation of localized regions of high heat transfer on both the upper and lower parts of the fin. Additionally, after flow separation near the tube, the recirculation zone forms become widely distributed, creating the largest low heat transfer area.

Compared to the other two shapes, the Gv shape (Figure 9c) provides a more uniform heat transfer distribution. While the reference shape and the reduced-pumping-power shape have locally high heat transfer coefficients at the end of the slits or locally low heat transfer coefficients at the middle of the slits, the Gv shape is generally uniform in this regard. In the area before the first row of tubes, the Gv shape exhibits a wide region of high heat transfer along the tube. Additionally, the flow directed below the slit immediately following the first row of tubes enhances the heat transfer coefficient compared to the other two shapes. Although low heat transfer areas appear after flow separation near the tubes, these areas are relatively narrow compared to the other two shapes. A low heat transfer area can also be observed at the end of the fin in the z-direction.

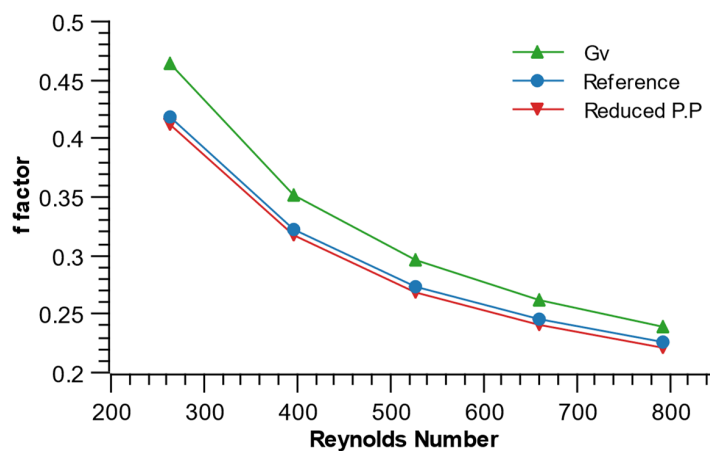
### 3.3. Performance Based on Geometry Optimization Using Objective Functions

#### 3.3.1. j- and f-Factor

The values of the j-factor according to velocity for the optimized shapes based on the objective functions are presented in Figure 10a. It is evident that the Gv shape has the highest j-factor at the same velocity. Compared to the reference shape, the j-factor of the Gv shape improved by an average of about 4.48%. It is about 5% higher than the reference shape at low velocities, but the performance improvement tends to decrease as the velocity increases. The reduced-pumping-power shape showed a decrease in the j-factor compared to the reference shape, with an average reduction of about 2.1%.



(a)



(b)

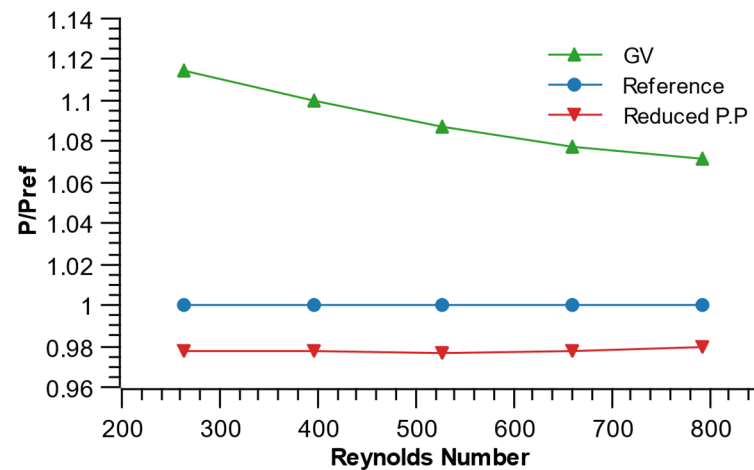
**Figure 10.** Comparison of heat transfer and friction coefficient vs. Reynolds number for optimized shapes and reference wavy-slit fin. (a) j-factor. (b) f-factor.

The values of the f-factor according to velocity for the optimized shapes are shown in Figure 10b. At the same velocity, the reduced-pumping-power shape has the lowest f-factor, with an average reduction of about 1.8% compared to the reference shape. In contrast, the Gv shape showed an average increase of 8.1% compared to the reference shape.

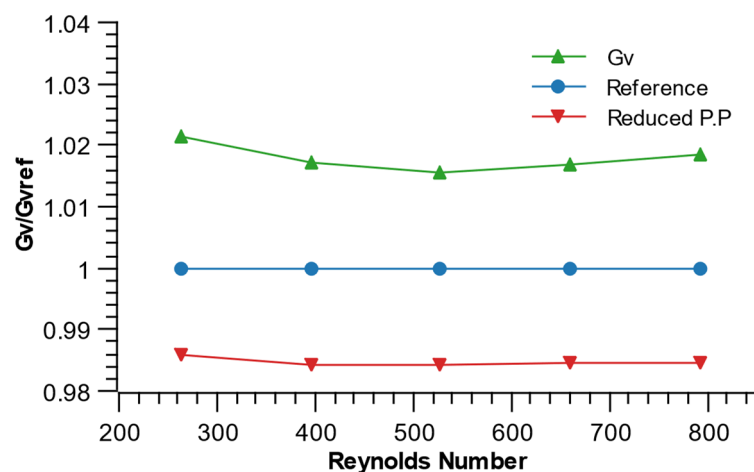
### 3.3.2. Performance Normalized to the Reference Shape

The average values in each region were calculated and non-dimensionalized using the baseline values for comparison to evaluate the performance improvements achieved through optimization. The values were determined based on the operating conditions, such as airflow rate, to verify whether the optimal shape for the design airflow rate also exhibited satisfactory performance under partial load conditions.

Figure 11a compares the pumping power for the three shapes. For the shape optimized for  $P$ , compared to the reference shape, the reduction trend remained constant within a range of 2% regardless of changes in the Reynolds number. However, for the Gv shape, as the airspeed decreased and the Reynolds number decreased,  $P$  increased by 7–11% compared to the reference shape. This was attributed to the definition of Gv: It is proportional to 1/3rd of the f-factor compared to the j-factor.



(a)



(b)

**Figure 11.** Performance variation with airflow rate for optimized shapes: pumping power and volume goodness factor. (a) Pumping power. (b) Volume goodness factor.

Figure 11b compares the volume goodness factor for the three shapes. For the shape optimized for  $P$ ,  $G_v$  remained constant at a value of 1.5% less than the reference shape across the changes in Reynolds number. The  $G_v$  shape showed a maximum improvement of 2% in  $G_v$  under the lowest airspeed conditions and a performance improvement of 1.8% under the maximum airspeed conditions.

#### 4. Conclusions

In the indoor unit of an air conditioner using low-GWP refrigerants, the optimization of the slit length, width, and height of wavy-slit fins did not yield any improvements in the objective functions [20]. To address this issue, we introduced the RSM to optimize the fin shape while taking into consideration the interactions that take place between different parameters. This approach enabled the determination of the optimal design for two objective functions: reduced pumping power and volume goodness factor. The flow and temperature fields were analyzed for each shape, and the performance metrics were evaluated. The key conclusions obtained from this analysis are as follows:

(1) In the regression model for pumping power, a local minimum was observed near the boundary of the design range with respect to the relationship between slit length and height, while an optimal point was anticipated outside the design range with respect to the relationship between slit length and width. For the relationship between slit height and width, a stationary point was identified at the boundary of the design range. In contrast, the regression model for the volume goodness factor best predicted the optimal point through a quadratic interaction between slit length and height. Additionally, a stationary point was observed at the midpoint between slit length and width, while another stationary point was found between slit height and width.

(2) In the model designed to minimize pumping power while maintaining a fixed heat transfer rate for the baseline configuration, the analysis of the flow and temperature fields revealed that the flow branching through the slits resulted in the vigorous mixing of the upper and lower surface flows, leading to a more uneven flow distribution. The largest separation zone was observed in the downstream flow of the duct. Although the pressure drop decreased, and the heat transfer rate declined to a minimal extent, under the design flow conditions, the heat transfer rate decreased by 0.55%, while the pumping power decreased by 2.05%. Additionally, the Colburn  $j$ -factor decreased by 2.11%, while the  $f$ -factor decreased by 1.78%. The reduction in pumping power was also maintained under partial load conditions.

(3) In the  $G_v$  optimization model, which aimed to maximize the volume goodness factor, the flow was divided into upper and lower branches after the duct through the slits was relatively uniform. The separation zone in the downstream flow of the duct was the smallest. Although the volume goodness factor improved, additional pumping power was required. Under the design flow conditions, the volume goodness factor increased by 1.85%, while the Colburn  $j$ -factor increased by 3.87%, and the  $f$ -factor increased by 6.09%. Under partial load conditions, the increase in pumping power was more significant.

Future work: The pumping power was not significantly influenced by the geometric parameter of slit width, resulting in only minor performance improvements. Moreover, the optimal point was found to be outside the geometric constraint range. This suggests the need for a study that includes the analysis of the effects of other dominant geometric variables, identifies the most influential parameters, and adjusts the experimental points using a sequential experimental design, such as the steepest ascent method, to develop a nonlinear model.

**Author Contributions:** J.R. and Y.K. carried out the simulations, analyzed the CFD data, and wrote the paper. J.A. supervised the research, analyzed the CFD data, and wrote the paper. All authors have read and agreed to the published version of the manuscript.

**Funding:** This work was supported by the Korea Institute of Energy Technology Evaluation and Planning (KETEP) grant funded by the Ministry of Trade, Industry and Energy (MOTIE) of the Republic of Korea (No. 20212020800070).

**Institutional Review Board Statement:** Not applicable.

**Informed Consent Statement:** Not applicable.

**Data Availability Statement:** The original contributions presented in the study are included in the article, further inquiries can be directed to the corresponding author.

**Conflicts of Interest:** The authors declare no conflict of interest.

## Nomenclature

$A_c$	Minimum flow cross-sectional area [m <sup>2</sup> ]
$A_0$	Area of heat exchanger [m <sup>2</sup> ]
$c_p$	Specific heat at constant pressure [kJ/(kg·K)]
$D_c$	Collar outer diameter [mm]
$F_s$	Fin pitch [mm]
$f$	Friction factor
$h$	Heat transfer coefficient [W/(m <sup>2</sup> ·K)]
$j$	Colburn j-factor
$L$	Slit length [mm]
$\dot{m}_{ac}$	Minimum area flow rate [kg/s]
$P$	Total pumping power per row [W/mm]
$P_l$	Longitudinal tube pitch [mm]
$P_t$	Transverse tube pitch [mm]
$Q$	Total heat duty per row [W/mm]
$Re$	Reynolds number
$St$	Stanton number
$V_m$	Maximum velocity [m/s]
$W$	Slit width [mm]
$H$	Slit height [mm]
$\Delta P$	Pressure drop [Pa]
$\Delta T$	Temperature difference [K]

### Greek Symbols

$\mu$	Viscosity [kg/(m·s)]
$\rho$	Density [kg/m <sup>3</sup> ]

## References

1. Masson-Delmotte, V.; Zhai, P.; Pirani, A.; Connors, S.L.; Péan, C.; Berger, S.; Caud, N.; Chen, Y.; Goldfarb, L.; Gomis, M.I. *Climate Change 2021: The Physical Science Basis; Contribution of Working Group I to the Sixth Assessment Report of the Intergovernmental Panel on Climate Change*; Cambridge University Press: Cambridge, UK, 2021.
2. Coulomb, D.; Dupont, J.; Morlet, V. *The Impact of the Refrigeration Sector on Climate Change-35 Informatory Note on Refrigeration Technologies*; IIF-IIR: Paris, France, 2017.
3. Beshr, M.; Aute, V.; Abdelaziz, O.; Fricke, B.; Radermacher, R. Potential emission savings from refrigeration and air conditioning systems by using low GWP refrigerants. *Int. J. Life Cycle Assess.* **2016**, *22*, 675. [[CrossRef](#)]
4. Khaleel, M.H.; Hassan, M.S.; Al-Oran, O.; Mohammed, S.O.; Najm, S.M. *Thermodynamic Evaluation of Low-GWP and Environmentally Friendly Alternative Refrigerants*; Canadian Center of Science and Education: Toronto, ON, Canada, 2024; Volume 12.
5. Wang, J.; Gullo, P.; Ramezani, H. Review on the trend of ultra-low-GWP working fluids for small-capacity vapour-compression systems. *Sustain. Energy Technol. Assess.* **2024**, *66*, 103803. [[CrossRef](#)]

6. Yao, Y.; Zhang, Z.; Hu, X. Experimental contrast on the cooling performance of direct evaporative all fresh air handling units with R32 and R410A. *Procedia Eng.* **2017**, *205*, 802–809. [[CrossRef](#)]
7. Saleem, S.; Bradshaw, C.R.; Bach, C.K. Development of design guidelines for fin-and-tube heat exchangers with low-GWP refrigerants. *Int. J. Refrig.* **2022**, *143*, 166–181. [[CrossRef](#)]
8. Wen, M.Y.; Ho, C.Y. Heat-transfer enhancement in fin-and-tube heat exchanger with improved fin design. *Appl. Therm. Eng.* **2009**, *29*, 1050–1057. [[CrossRef](#)]
9. Sadeghianjahromi, A.; Wang, C. Heat transfer enhancement in fin-and-tube heat exchangers—A review on different mechanisms. *Renew. Sustain. Energy Rev.* **2020**, *137*, 110470. [[CrossRef](#)]
10. Shah, R.K.; Metzger, D.E.; London, A.L.; Kraus, A.D. *Compact Heat Exchangers*; Hemisphere Pub. Corp: New York, NY, USA, 1990.
11. Yun, J.Y.; Lee, K.S. Investigation of heat transfer characteristics on various kinds of fin-and-tube heat exchangers with interrupted surfaces. *Int. J. Heat Mass Transf.* **1999**, *42*, 2375–2385. [[CrossRef](#)]
12. Youn, B.; Kim, N.H. An experimental investigation on the airside performance of fin-and-tube heat exchangers having sinusoidal wave fins. *Heat Mass Transf.* **2006**, *43*, 1249–1262. [[CrossRef](#)]
13. Yoon, B.; Gil, Y.H.; Park, H.Y.; Kim, Y.S. Experimental study of air side pressure drop and heat transfer characteristics of wave and wave-slit fin-tube heat exchangers. *Korean J. Air-Cond. Refrig. Eng.* **1998**, *10*, 589–599.
14. Mohanta, L.; Joardar, A.; Esformes, J.L.; Videto, B.; Siemel, T.H. Numerical analysis of fluid flow and heat transfer in wavy and hybrid-slit-wavy fin-and-tube heat exchangers. *Sci. Technol. Built Environ.* **2019**, *25*, 767. [[CrossRef](#)]
15. Aslam Bhutta, M.M.; Hayat, N.; Bashir, M.H.; Khan, A.R.; Ahmad, K.N.; Khan, S. CFD applications in various heat exchangers design: A review. *Appl. Therm. Eng.* **2012**, *32*, 1–12. [[CrossRef](#)]
16. Liu, X.; Wang, M.; Liu, H.; Chen, W.; Qian, S. Numerical analysis on heat transfer enhancement of wavy fin-tube heat exchangers for air-conditioning applications. *Appl. Therm. Eng.* **2021**, *199*, 117597. [[CrossRef](#)]
17. Li, W.; Khan, T.A.; Tang, W.; Minkowycz, W.J. Numerical study and optimization of corrugation height and angle of attack of vortex generator in the wavy fin-and-tube heat exchanger. *J. Heat Transf.* **2018**, *140*, 111801. [[CrossRef](#)]
18. Sadeghianjahromi, A.; Kheradmand, S.; Nemati, H.; Wang, C. Heat transfer enhancement of wavy fin-and-tube heat exchangers via innovative compound designs. *Int. J. Therm. Sci.* **2020**, *149*, 106211. [[CrossRef](#)]
19. Lee, S.; Ahn, J. The air-side thermal hydraulic performance analysis of slit wavy fin-tube heat exchanger with small diameter using CFD. *KSME-B* **2022**, *46*, 603. [[CrossRef](#)]
20. Park, S.; Kang, H.; Ahn, J. Air-side performance analysis by geometric parameters of hybrid-wave-slit fin using CFD. *KSME-B* **2024**, *48*, 361. [[CrossRef](#)]
21. Khuri, A.I.; Cornell, J.A. *Response Surfaces: Designs and Analyses*; CRC press: Boca Raton, FL, USA, 2018.
22. Myers, R.H.; Montgomery, D.C.; Anderson-Cook, C.M. *Response Surface Methodology: Process and Product Optimization Using Designed Experiments*; John Wiley & Sons: Hoboken, NJ, USA, 2016.
23. Soland, J.G.; Mack, M.G., Jr.; Rohsenow, W.M. Performance ranking of plate-fin heat exchange surfaces. *J. Heat Transf.* **1978**, *99*, 110.
24. Webb, R.L.; Kim, N. *Principles of Enhanced Heat Transfer*; Taylor & Francis: Boca Raton, FY, USA, 2005.
25. Jeong, C.H.; Kim, H.R.; Ha, M.Y.; Son, S.W.; Lee, J.S.; Kim, P.Y. Numerical investigation of thermal enhancement of plate fin type heat exchanger with creases and holes in construction machinery. *Appl. Therm. Eng.* **2013**, *62*, 529. [[CrossRef](#)]
26. Lei, Y.; He, Y.; Tian, L.; Chu, P.; Tao, W. Hydrodynamics and heat transfer characteristics of a novel heat exchanger with delta-winglet vortex generators. *Chem. Eng. Sci.* **2009**, *65*, 1551. [[CrossRef](#)]
27. Ansys, I. Ansys Fluent Theory Guide. *Ansys Inc. USA* **2011**, 15317, 724–746.
28. Wilcox, D.C. *Turbulence Modeling for CFD*; DCW Industries: La Canada, CA, USA, 1998.
29. Florian, R.M. Zonal two-equation k- $\omega$  turbulence models for aerodynamic flows. In Proceedings of the 24th AIAA Fluid Dynamic Conference, Orlando, FL, USA, 6–9 July 1993.
30. Harrison, X.A.; Donaldson, L.; Correa-Cano, M.E.; Evans, J.; Fisher, D.N.; Goodwin, C.E.D.; Robinson, B.S.; Hodgson, D.J.; Inger, R. A brief introduction to mixed effects modelling and multi-model inference in ecology. *PeerJ* **2018**, *6*, e4794. [[CrossRef](#)]

**Disclaimer/Publisher’s Note:** The statements, opinions and data contained in all publications are solely those of the individual author(s) and contributor(s) and not of MDPI and/or the editor(s). MDPI and/or the editor(s) disclaim responsibility for any injury to people or property resulting from any ideas, methods, instructions or products referred to in the content.